

Multiphysics Finite Element Modeling of Irradiation and Thermal Behavior Demonstrated on a Fuel-Assembly Problem

Fabrizio Aguzzi^a, Martín Armoa^a, Santiago M. Rabazzi^a, César Pairetti^{a,c} and Alejandro E. Albanesi^{b,*}

^aIFIR Instituto de Física de Rosario, CONICET-UNR, Ocampo y Esmeralda, Predio CONICET Rosario, 2000, Argentina

^bCIMEC Centro de Investigación de Métodos Computacionales, CONICET-UNL, Col. Ruta 168 s/n, Predio CONICET Santa Fe, 3000, Argentina

^cSorbonne Université and CNRS, UMR 7190, Institut Jean Le Rond d'Alembert, Paris, 75005, France

ARTICLE INFO

Keywords:

Thermal creep
Spacer-cladding interaction
Zircaloy-2
Polycrystalline modeling
Code_Aster
VPSC
Thermo-mechanical simulation

ABSTRACT

This work presents a modeling framework to represent the thermomechanical behavior of complex materials, based on micro mechanical dynamics. This tool is then applied to fuel rod elements, consisting of Zircaloy-2 cladding tubes and spacer grids, under typical Pressurized Water Reactor (PWR) conditions. The model incorporates thermal expansion and thermal creep through a VPSC-FEM coupling with the finite element (FEM) solver Code_Aster, enabling analysis of in-reactor behavior under combined thermal, mechanical, and irradiation loading. The framework captures anisotropic deformation driven by crystallographic texture and prismatic slip activity under radial loading. Thermal creep, being stress-sensitive, contributes to early-stage stress relaxation and strain accumulation, leading to higher strain compared to the irradiation-only case. The interaction of thermal creep with irradiation mechanisms was found to modify the stress distribution and clearance evolution, with relaxation governed by prismatic slip. For fuel rod elements, irradiation-induced mechanisms dominate the long-term clearance behavior, whereas thermal effects remain relevant in contact dynamics during thermal preloading. Furthermore, the stress-strain response was found to be more sensitive to micromechanics than to elasticity. This high-resolution formulation enables predictive modeling of spacer-cladding interaction and provides a basis for the development of reduced-order models.

1. Introduction


Understanding the mechanical behavior of zirconium alloys under irradiation is essential for predicting the performance and integrity of nuclear fuel cladding. Deformation in zirconium alloys during in-reactor operation is driven by three concurrent mechanisms: thermal creep, irradiation creep, and irradiation-induced growth (Adamson et al., 2019; Carpenter et al., 1988; Fidleris, 1988; Holt, 2008; Onimus et al., 2020; Rogerson, 1988). While irradiation-induced effects are dominant in most high-flux regions, thermal phenomena cannot be neglected, particularly under steady-state or transient conditions where elevated temperatures may activate additional creep mechanisms.

Thermal creep in zirconium alloys typically becomes significant above 523–623 K, depending on the alloy composition, stress level, and microstructural condition. In unirradiated materials, this phenomenon is governed by well-known diffusional processes. However, under neutron irradiation, the microstructural evolution substantially modifies the creep response. This process involves the formation of point defects, loops, and dislocation structures. As a result, extrapolations from ex-reactor data may be unreliable. Moreover, in low-flux regions (e.g., near fuel rod extremities), thermal creep can remain active for extended periods, contributing significantly to strain accumulation (Adamson et al., 2009, 2019).

Moore et al. (Moore et al., 2025) emphasized the intricate interplay between irradiation and thermal creep, noting that these mechanisms—although often assumed additive and independent—operate simultaneously under reactor conditions, complicating the interpretation of dimensional changes. While irradiation creep is generally considered athermal, weakly dependent on temperature, thermal creep becomes increasingly relevant at elevated temperatures. This distinction is particularly important in scenarios involving Pellet-Cladding Mechanical Interaction (PCMI), such as during power ramps, where localized overheating can trigger thermal creep. These observations highlight the pressing need for comprehensive, physically-based models that incorporate both irradiation and thermal effects to accurately capture their respective contributions to fuel cladding deformation.

Despite extensive work on creep modeling in zirconium alloys, many contributions have focused on pressure tubes in heavy-water reactors or on cladding tubes under simplified loading conditions. Phenomenological macroscopic models, derived from experimental campaigns, have been widely used to study internal/external pressure, temperature, anisotropy, and irradiation effects (Murty, 1999; Matsuo, 1987). However, these models are often limited in scope and typically valid only within specific parameter ranges. Several researchers (Christodoulou et al., 1996; Limback and Andersson, 1996) have proposed empirical approaches where deformation mechanisms are added at the macroscopic level without explicitly accounting for the polycrystalline structure of the material.

*Corresponding author

 aalbanesi@cimec.santafe-conicet.gov.ar (A.E. Albanesi)

ORCID(s):

Due to their technological importance and strong plastic anisotropy, zirconium alloys have received considerable attention since the seminal work by Woo (1985). Subsequent studies explored the anisotropic response under irradiation using polycrystalline models and homogenization techniques, focusing on irradiation creep and growth (Carpenter et al., 1988; Lebensohn and Tomé, 1993; Turner and Tomé, 1993; Tomé et al., 1993; Turner et al., 1994; Tomé et al., 1996; Turner et al., 1999; Christodoulou et al., 2002; Patra et al., 2017a; Montgomery et al., 2017). Although similar micromechanical approaches have also been proposed for modeling thermal creep (Brenner et al., 2002), their application remains limited.

More recently, Fast Fourier Transform (FFT)-based methods have been employed to study the combined effects of irradiation and thermal mechanisms in polycrystalline aggregates of Zircaloy-4 (Onimus et al., 2020, 2022; Gicquel et al., 2023). These grain-level simulations reinforce the need for physically-based models capable of capturing microstructural effects, crystallographic texture, and the directional nature of slip and growth processes.

Building upon this perspective, the present work introduces an extended polycrystalline constitutive framework based on the VPSC model, coupled with the finite element code Code_Aster (EDF, 1989–2025) via the CAFEM-VPSC interface (Aguzzi et al., 2025). The current model incorporates two additional thermally activated mechanisms, thermal creep and thermal expansion, enabling a more comprehensive and realistic simulation of in-reactor deformation in Zircaloy-2.

In section 3 of this manuscript, this framework is employed to simulate the non-linear evolution of the clearance between the cladding tube and spacer grid under Pressurized Water Reactor (PWR) conditions. This analysis aims to assess the relative importance of thermal and irradiation effects by applying a comprehensive material description based on a micromechanical approach. In section 4, a detailed description of the stress and strains shows the impact of each micromechanical phenomenon on the global behavior of the assembly. By capturing the coupled response of Spacer-Cladding Interaction (SCI), the study enhances the predictive capabilities of computational tools for evaluating fuel rod performance and structural integrity under realistic reactor operation.

2. Multiphysics Simulation Methodology

2.1. Micro-Scale Model

2.1.1. Irradiation-Induced Growth

We apply a model based in a reaction-diffusion formulation, following Patra et al. (2017b). In this context, the strain-rate tensor due to irradiation-induced growth is obtained by linear superposition over the crystallographic directions $j \in \{\mathbf{a}_1, \mathbf{a}_2, \mathbf{a}_3, \mathbf{c}\}$:

$$\dot{\epsilon}_{kl}^{(\text{growth})} = \sum_{j \in \{\mathbf{a}_1, \mathbf{a}_2, \mathbf{a}_3, \mathbf{c}\}} \dot{\epsilon}_{\text{growth}}^j b_k^j b_l^j, \quad k, l \in \{\mathbf{x}, \mathbf{y}, \mathbf{z}\},$$

(1)

where b_k^j and b_l^j are the components of the Burgers vector \mathbf{b}^j along the crystal-axis directions \mathbf{k} and \mathbf{l} , respectively. Each deformation rate $\dot{\epsilon}_{\text{growth}}^j$ is the sum of effects from dislocation-climb and grain-boundary-absorption induced growths:

$$\dot{\epsilon}_{\text{growth}}^j = \dot{\epsilon}_{\text{climb}}^j + \dot{\epsilon}_{\text{GB}}^j, \quad j \in \{\mathbf{a}_1, \mathbf{a}_2, \mathbf{a}_3, \mathbf{c}\}, \quad (2)$$

where the $\dot{\epsilon}_{\text{climb}}^j$ is defined based on the defect production rate from vacancies and interstitials, following Norgett et al. (1975), and $\dot{\epsilon}_{\text{GB}}^j$ follows an equivalent rationale for grain boundaries, as described in Aguzzi et al. (2025).

2.1.2. Irradiation-induced creep crystallography model

The growth of one grain under irradiation can be interrupted by the growth of a neighbouring grain. This incompatibility creates internal stresses known as creep under irradiation. Irradiation creep is intrinsically coupled with irradiation-induced growth, occurring independent of external loads.

Our analysis uses the crystallographic irradiation creep model for steels (Foster et al. (1972), Ehrlich (1981)) as implemented by Patra et al. (2017b), with swelling effects disregarded. This constitutive law models the creep strain rate as linearly proportional to both applied stress and radiation dose rate $\frac{d\phi}{dt}$, expressed in terms of effective stress and strain components:

$$\dot{\epsilon}^{\text{creep}} = B_0 \sigma \frac{d\phi}{dt}; \quad (3)$$

effective stress is denoted by σ , B_0 is the irradiation creep compliance, and $\frac{d\phi}{dt}$ is the radiation dose rate (in $\text{dpa} \cdot \text{s}^{-1}$). A similar phenomenological law is assumed to represent the shear rate associated with irradiation creep at the level of slip systems, as:

$$\dot{\gamma}_{\text{creep}}^j = B \frac{\rho_d^j}{\rho_{\text{ref}}} \tau^j \frac{d\phi}{dt}; \quad (4)$$

where B is the crystallographic irradiation creep compliance, τ^j is the resolved shear stress on slip system j , and ρ_{ref} is the reference line dislocation density. The crystallographic shear rate is a function of the resolved shear stress τ^j and of the line dislocation density ρ_d^j gliding on slip system j . The anisotropic creep arises from the distribution of dislocations among the slip systems, such that the creep strain rate (and its associated relaxation) is greater in systems with higher dislocation density. The normalization factor ρ_{ref} ensures that the crystallographic irradiation creep compliance B has the same physical units as the macroscopic compliance B_0 used in Eq. 3. The specific values for the irradiation creep model parameters adopted in this work are provided in Appendix A and were taken from Patra et al. (2017b).

2.1.3. Thermal Creep Model

Thermal creep is a phenomenon associated with the motion of dislocations that overcome obstacles via temperature- and stress-activated diffusion mechanisms. Although this process becomes more pronounced at elevated temperatures ($T > 0.5T_M$, being T_M the melting temperature), or under stresses close to the yield strength ($\sigma > 0.75\sigma_f$), it is not limited to abnormal or accidental conditions. Experimental tests under steady-state conditions have demonstrated that this mechanism can also be activated within the normal operating range of nuclear reactors, with significant effects on material behavior (Christodoulou et al., 2002; Fidleris, 1988; Xiao et al., 2023).

The power-law expression in Eq. 5 is suitable for describing the contribution of multiple slip systems to the total creep within a grain:

$$\dot{\epsilon}_{ij}^{\text{thcreep}} = \sum_s m_{ij}^s \dot{\gamma}^s = \dot{\gamma}_0(T) \sum_s m_{ij}^s \left(\frac{m_{ij}^s \sigma_{kl}}{\tau_{\text{thres}}^s} \right)^n; \quad (5)$$

In the expression given by Eq. 5, m_{ij}^s is the Schmid tensor, defined as $m_{ij}^s = \frac{1}{2}(b_i^s n_j^s + b_j^s n_i^s)$, where \mathbf{n}^s is the normal to the slip plane, and \mathbf{b}^s is the slip direction (Burgers vector) of the s -th slip system. Slip may occur on prismatic, basal, or pyramidal planes (see Section 2.2.1). The parameters in Eq. 5 are related to the physical properties of Zr alloys and are detailed in the following paragraphs.

The reference shear rate $\dot{\gamma}_0$ depends on temperature and the activation energy of the diffusion mechanism that controls the process. For this study, we adopt the temperature dependence proposed in Christodoulou et al. (2002), derived from the fitting of an extensive experimental database from tensile and shear creep tests on Zr-2.5%Nb alloy tubes under various stresses, temperatures, and directions. In that work, $\dot{\gamma}_0$ is assumed identical for all slip systems, an idealization, and the creep behavior of each system is distinguished by its threshold stress τ_{thres}^s . Those authors report:

$$\dot{\gamma}_0(T) = \dot{\gamma}_0(T = 523\text{K}) \exp \left[-Q(T) \left(\frac{1}{T} - \frac{1}{523} \right) \right], \quad (6)$$

where $\dot{\gamma}_0(T = 523\text{K}) = 4.157 \times 10^{-7} \text{ h}^{-1}$, and

$$Q(T) = \left(5000 + \frac{5600}{1 + \exp\left(-\frac{T-470}{15}\right)} \right), \quad (7)$$

Experimental studies report a wide range of thermal creep parameters for zirconium alloys, reflecting their sensitivity to alloy composition, temperature, and stress levels. The rate sensitivity exponent n typically ranges from 3.4 to 5.0, although values as high as 100 have been reported under high-stress regimes (Christodoulou et al., 2002; Wang et al., 2013; Hayes and Kassner, 2006; Franklin et al., 1983). Pre-exponential factors $\dot{\gamma}_0$ also vary significantly, with values on the order of 10^{-8} s^{-1} reported in the literature (Onimus et al., 2022). These variations highlight the need to calibrate model

parameters according to the specific material and loading conditions.

In this work, we adopt $n = 4$ and use threshold resolved shear stresses of 0.100 GPa (prismatic), 0.111 GPa (basal), and 0.300 GPa (pyramidal). Other experimental datasets, such as those in (Butcher and Donohue, 1986), can be used to fit and validate the model under irradiation conditions.

2.1.4. Crystallographic Model for Thermal Expansion

A temperature change induces a resulting strain in the material. Under certain conditions, the components of the thermal strain tensor are proportional to the temperature increment:

$$\epsilon_{ij}^{\text{therm}} = \alpha_{ij} \Delta T \quad (8)$$

where α_{ij} are the thermal expansion coefficients of the material. These coefficients are generally positive, although negative values have been reported in specific cases (Sleight, 1998). Moreover, thermal expansion coefficients are strongly temperature dependent.

The thermal expansion coefficients used for zirconium in this study were $\alpha_{A;Ro} = 5.4$, $\alpha_{H;Tr} = 9.1$, and $\alpha_{R;No} = 7.4$, all expressed in units of 10^{-6} K^{-1} . The subscripts refer to the axial (A), hoop (H), and radial (R) directions of the cladding tube, as well as the rolling (Ro), transverse (Tr), and normal (No) directions of the spacer grid dimples, which are defined according to the crystallographic texture shown in Fig. 3. These values are based on experimental measurements reported by Goldak et al. (1966).

For the simulations, the elastic constants reported by Simmons (1965); Kocks et al. (2000) were adopted. At room temperature, the values used were:

$$\begin{aligned} C_{11} &= 143.5 \text{ GPa}, & C_{33} &= 164.9 \text{ GPa}, \\ C_{44} &= 32.1 \text{ GPa}, & C_{12} &= 72.5 \text{ GPa}, & C_{13} &= 65.4 \text{ GPa}. \end{aligned}$$

These values reflect the strong elastic and thermal anisotropy of zirconium, which plays a key role in transient scenarios and must be properly accounted for in predictive modeling.

2.2. Meso-Scale Model

2.2.1. Viscoplastic Self-Consistent Model (VPSC)

The VPSC model (Molinari et al., 1987; Tomé et al., 1993) has been extended over time to include creep and irradiation growth at the grain scale, considering texture and grain interactions (Patra et al., 2017b; Tomé and Lebensohn, 2023). In this work, it is further developed to incorporate thermal creep and thermal expansion, given by Eqs. (5), (8), respectively, enhancing its ability to simulate the thermomechanical behavior of zirconium alloys under reactor conditions.

The total deformation rate at the grain level is given by the contribution of the phenomena mentioned above: (1,3,5,8):

$$\dot{\epsilon}_{ij} = \dot{\epsilon}_{ij}^{(\text{growth})} + \dot{\epsilon}_{ij}^{(\text{creep})} + \dot{\epsilon}_{ij}^{(\text{thcreep})} + \dot{\epsilon}_{ij}^{(\text{therm})} \quad (9)$$

The VPSC code can be executed under different linearization schemes, and the corresponding results may differ significantly when using the same hardening parameters Tomé and Lebensohn (2023). For the response of the effective medium (polycrystal), the tangent linearization was used in this work:

$$\bar{\epsilon}_{ij} = \bar{M}_{ijkl} \bar{\sigma}_{kl} + \bar{\epsilon}_{ij}^0 \quad (10)$$

where $\bar{\epsilon}_{ij}$ and $\bar{\sigma}_{kl}$ represent the average (macroscopic) strain rate and stress, respectively. \bar{M}_{ijkl} denotes the macroscopic creep compliance, while $\bar{\epsilon}_{ij}^0$ corresponds to the macroscopic strain rate resulting from irradiation-induced growth. These macroscopic quantities, \bar{M}_{ijkl} and $\bar{\epsilon}_{ij}^0$ are initially unknown and must be determined self-consistently by enforcing that the volume-averaged stress and strain rate over all grains match those of the effective medium, namely:

$$\bar{\epsilon}_{ij} = \langle \dot{\epsilon}_{ij}^c \rangle; \quad \bar{\sigma}_{kl} = \langle \sigma_{kl}^c \rangle \quad (11)$$

Previous applications of the self-consistent polycrystalline model focused on simulating creep and irradiation-induced growth in hexagonal materials Tomé et al. (1996); Turner et al. (1999), but did not incorporate the time evolution of microstructural changes. In this study, we build upon that framework by introducing time-dependent formulations for both creep and irradiation growth. While Patra et al. (2017a) implemented this on a proprietary FEM solver, our approach is implemented within Code_Aster EDF (1989–2025), an open-source FEM solver suited for nuclear engineering problems.

Regarding thermal phenomena, Montgomery et al. (2017) incorporated thermal creep but did not consider thermal expansion. In contrast, our current formulation includes both thermal creep and thermal expansion at the grain level. In summary, the toolbox integrating Code_Aster and VPSC to model irradiation creep and growth, developed in Aguzzi et al. (2025), has been expanded to also incorporate thermal creep and thermal expansion, resulting in a more versatile and comprehensive model to analyze the nonlinear contact between grid and cladding.

2.2.2. Sensitivity Analysis of Thermal Effects

Although thermal creep and thermal expansion typically induce smaller strains than irradiation effects, their contribution becomes relevant under reactor operating conditions due to elevated temperatures and their role in stress relaxation. These thermally activated mechanisms help redistribute stresses and influence the overall deformation behavior, particularly in textured materials such as Zircaloy-2.

Figure 1 highlights the dependence of thermal creep on the applied stress to the cladding tube. The curves show the axial strain evolution at 523 K for different axial loads (0, 50, 100, 150, 200 MPa). Solid lines represent the strain induced by irradiation effects only (creep and growth), while

dashed lines show the total axial strain when thermal creep and thermal expansion are also included. These results were obtained using the VPSC stand-alone (VPSC-SA) code, without integration to the finite element solver. The results clearly demonstrate that, for a given stress level, the total strain is consistently higher when thermal effects are considered—indicating the stress-sensitive nature of thermal creep.

This observation is consistent with the thermal creep formulation in Eq. 5, where the strain rate is proportional to the stress raised to a power n (typically $n = 4$ for Zircaloy). Although the temperature dependence enters through the prefactor $\dot{\gamma}_0(T)$ in Eq. 6, its exponential variation is much slower compared to the polynomial amplification of stress. This illustrates that, under typical PWR conditions, thermal creep is significantly more sensitive to stress than to temperature variations.

This behavior is closely related to the crystallographic texture. As shown in Fig. 3(a), the predominance of prismatic planes aligned with the axial and hoop directions facilitates thermal creep along those directions due to their lower critical resolved shear stress. Under compressive radial loading (e.g., from external pressure), these slip systems efficiently accommodate plastic deformation, thereby contributing to stress relaxation.

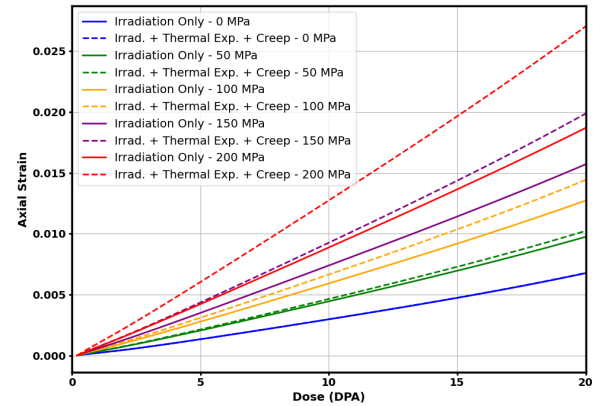


Fig. 1: Axial strain as a function of axial load for the texture shown in Fig. 3(a), considering either irradiation creep alone or the combined effects of irradiation creep and thermal creep (including thermal expansion for heating rate= 0.0018K/h).

2.3. Macro-Scale Model

2.3.1. VPSC-CAFEM interaction framework

The VPSC-CAFEM interface integrates the polycrystalline constitutive model VPSC with the finite element solver Code_Aster (Aguzzi et al., 2025). At each time increment, the solver provides the strain increment $\Delta\epsilon_{FE}$, the time step Δt , and a rotation matrix R defining the local coordinate system.

The total strain increment is decomposed into elastic and viscoplastic contributions:

$$\Delta\epsilon = \Delta\epsilon^e + \Delta\epsilon^{vp} = C^{-1} : \Delta\sigma + \Delta\epsilon^{vp} \quad (12)$$

The viscoplastic strain results from mechanisms such as irradiation creep and thermal creep (stress-dependent), as well as irradiation growth and thermal expansion (stress-independent). These contributions depend on the current stress σ and internal state variables, such as grain orientations and hardening parameters.

To ensure consistency with the local frame used in Code_Aster, stress and strain tensors are rotated using:

$$\Delta \epsilon^* = \mathbf{R} \Delta \epsilon \mathbf{R}^T, \quad \sigma^* = \mathbf{R} \sigma \mathbf{R}^T \quad (13)$$

The superscript $*$ indicates quantities in the local coordinate system. A Newton-Raphson iterative scheme is employed to solve for the updated stress. The residual function, defined as the difference between the strain of the constitutive model and the strain provided by the FEM solver (Segurado et al., 2012), is given by:

$$\mathbf{X}(\Delta \sigma^*) = \Delta \epsilon^* - \Delta \epsilon_{FE}^* = \mathbf{C}^{-1} : \Delta \sigma^* + \dot{\epsilon}^{vp*} \Delta t - \Delta \epsilon_{FE}^* \quad (14)$$

The stress increment is updated iteratively as:

$$(\Delta \sigma^*)_{k+1} = (\Delta \sigma^*)_k - \mathbf{J}_{NR}^{-1}((\Delta \sigma^*)_k) : \mathbf{X}((\Delta \sigma^*)_k) \quad (15)$$

where the Newton-Raphson Jacobian $\mathbf{J}_{NR}^* = \mathbf{C}^{-1} + \mathbf{M} \Delta t$ includes the elastic stiffness \mathbf{C} and the viscoplastic tangent modulus \mathbf{M} provided by the VPSC model.

Upon convergence, the stress tensor and the consistent tangent operator are rotated back to the global coordinate system to ensure compatibility with the Code_Aster solver:

$$\sigma^{t+\Delta t} = \mathbf{R}^T \sigma^{t+\Delta t*} \mathbf{R}, \quad \mathbf{C}^{tg} = \mathbf{R} \mathbf{C}^{tg*} \mathbf{R}^T \quad (16)$$

Here, \mathbf{R} denotes the fourth-order rotation tensor derived from the second-order rotation matrix \mathbf{R} . The component-wise transformation of the consistent tangent operator is given by:

$$C_{ijkl}^{tg} = R_{im} R_{jn} R_{ko} R_{lp} C_{mnop}^{tg*} \quad (17)$$

Convergence is monitored by evaluating a weighted norm of the residual (McGinty, 2001):

$$\chi = \sqrt{\sum_{ij} \left(\frac{|\Delta \epsilon_{FE}^{ij}|}{\max(|\Delta \epsilon_{FE}^{ij}|)} X^{ij} \right)^2} \quad (18)$$

A validation of this coupling strategy, including comparison with stand-alone VPSC results, is provided in Appendix B.

3. Mechanical Contact Analysis in Spacer Grid-Cladding Systems

The simulation domain consists of a reduced model comprising half of the cladding tube and a portion of the central

hexagon of the spacer grid, a common design in PWRs. Representative images of the spacer grid structure are available on the official CONUAR website (CONUAR, 2025). This simplification, based on geometric symmetry (Fig. 2), significantly reduces computational cost while maintaining the physical representativeness of the contact problem. The spacer grid includes four dimples that interact with the tube surface, and a representative spring force of 45 N ensures initial mechanical contact.

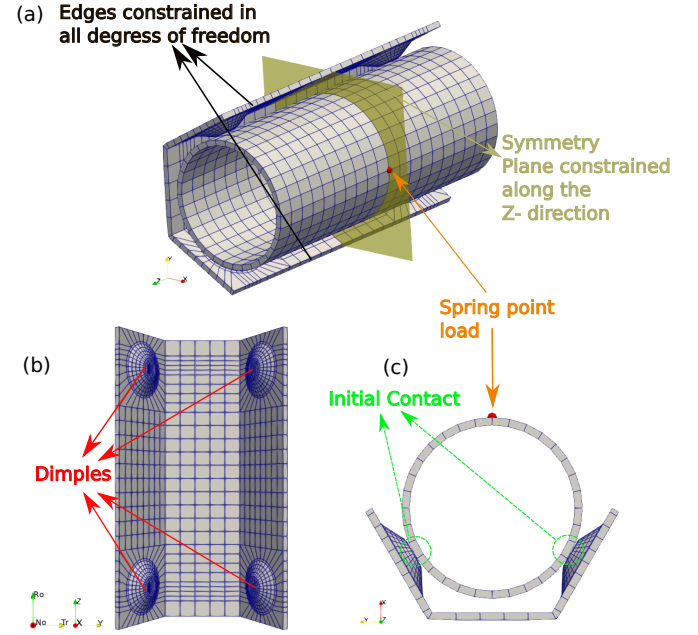


Fig. 2: (a) Cladding tube-grid assembly. (b) Front view of the grid with four supporting dimples. The bottom-left corner shows the coordinate system for the grid sheet. (c) Top view showing the spring contact force on the cladding tube.

The assembly was subjected to constant in-reactor conditions: 523 K temperature, 15.5 MPa external coolant pressure, and 10 MPa internal pressure. A uniform irradiation dose rate of $3.6 \times 10^{-4} \text{ dpa} \cdot \text{hr}^{-1}$ was applied for 100 increments of 555.6 hours each. No additional external loads were imposed; however, the pressure differential introduces circumferential and axial stresses in the structure.

To balance fidelity and efficiency in the VPSC-CAFEM coupling, a reduced texture approach was used (Aguzzi et al., 2025; Patra et al., 2017a), assigning 7 grain orientations to the cladding tube and 13 to the spacer dimples (Fig. 3). The cold-worked Zircaloy-2 model was calibrated against irradiation growth data at 550 K (Holt et al., 1996).

Boundary conditions imposed axial constraints at the base of the tube (allowing radial displacement), and full fixation of the lateral dimple-edge nodes to eliminate rigid body motion. A preliminary elastic step ensured contact formation without irradiation or thermal loads. Once established, the simulation switched to a nonlinear contact model including irradiation and thermal phenomena, using crystallographic textures.

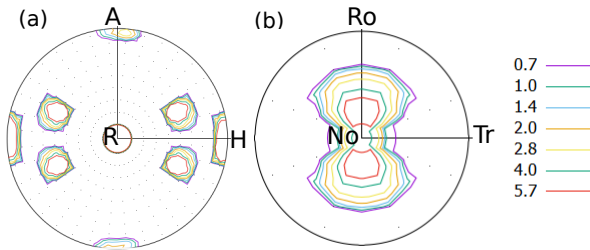


Fig. 3: Basal pole figures of the reduced textures used in the simulation. (a) Cladding tube: 7 orientations aligned with axial (A), hoop (H), and radial (R) directions. (b) Spacer dimples: 13 orientations with rolling (Ro), transverse (Tr), and normal (No) directions.

Contact was modeled using a node-to-segment master–slave algorithm implemented in Code_Aster (U2.04.04, 2024). The cladding tube was defined as the master surface and the grid as the slave. Friction was neglected to isolate mechanical effects. This strategy enables accurate capture of local displacements and stress gradients—improving upon classical methods based on uniform displacement or predefined gap—and allows the clearance (CLR) variable to track component separation throughout the simulation.

4. Numerical results and analysis

This section presents the results obtained with the open-source toolbox that integrates Code_Aster and VPSC to model irradiation creep and growth, and in particular the implementation of thermal creep and thermal expansion.

4.1. Evolution of contact opening

In this study, a nonlinear contact analysis is conducted using Code_Aster to enable a node-by-node evaluation of contact zones, accounting for differential displacements and stress distributions at meso- and macroscopic scales. Such modeling approach significantly improves the accuracy of predictions for contact stresses and separation phenomena compared to conventional rigid-body frameworks, as it captures spatially resolved interactions governed by material and geometric nonlinearities. Fig. 4 shows the contact surfaces under analysis. Considering an orientation in which the X-axis emerges perpendicularly from the plane, the contact located on the left is referred to as "Side 1", while the contact on the right is identified as "Side 2".

Figure 5 shows the evolution of the maximum CLR under different physical mechanisms. The curves represent the individual and combined contributions of irradiation growth, irradiation creep, thermal expansion, and thermal creep. All simulations were performed using the crystallographic textures shown in Fig. 3.

This value corresponds to the highest CLR among all nodes, specifically at the peripheral nodes of the slave surface of the dimple, where the separation from the cladding tube is greatest (see red area in Fig. 4). The cladding tube element in contact with the dimple surface undergoes a

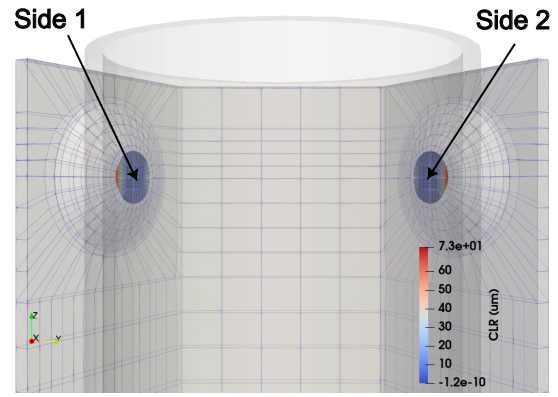


Fig. 4: CLR corresponding to the slaves surfaces for non-linear contact for 20 dpa and 523K.

pivoting motion around the region of highest contact (and therefore highest stress) until it fully adjusts. At a dose above 1.2 dpa, the components of slides 1 and 2 begin to separate due to the deformation mechanisms described in Section 2.2.2 for the irradiation and thermal creep.

Although experimental data on in-reactor CLR remains scarce, prior reactor investigations typically report values between 10 and 30 μm for grid-to-rod contact Joulin et al. (2002); Jiang et al. (2016); Billerey (2005); Patra et al. (2017a). These values refer to the change in clearance, i.e., the difference between the final and initial separation. The present work extends previous modeling approaches by integrating thermal effects and capturing the combined contribution of irradiation growth, irradiation creep, thermal expansion, and thermal creep at the crystal scale. By explicitly resolving crystallographic textures and slip system activity, the model offers a more physically realistic prediction of CLR evolution under operational conditions, reinforcing its potential as a robust multiscale tool for spacer-cladding interaction analysis.

4.2. Combined thermal and irradiation effects

The analysis of this section studies the influence of thermal and irradiation-induced phenomena on the contact and separation behavior between the cladding tube and the spacer grid. To this end, five numerical simulations were performed: four isolating each physical phenomenon individually, and one combining all phenomena simultaneously.

Although from a physical point of view the decoupling of these mechanisms is not strictly realistic—since all are inherently present and interacting during operation—this separation allows for a clearer understanding of the individual contribution of each mechanism to the evolution of the CLR.

Figure 5 summarizes the individual and combined effects of the physical mechanisms on CLR evolution. The simulation with only *irradiation growth* (blue symbols) shows a rapid initial approach between tube and grid, stabilizing up to approximately 7.5 dpa, after which a linear

separation trend begins. This is attributed to anisotropic lattice deformation: contraction along the c -axis and expansion along the a -axes of the HCP zirconium lattice. As shown in Fig. 3, the alignment of basal poles enhances this radial expansion.

In the case of *thermal expansion*, a constant heating rate of 1.799×10^{-5} K/h (i.e., $\Delta T = 1$ K over the simulation) was applied. The CLR remains nearly constant for about 45,000 hours, followed by a slight reduction (down to $65 \mu\text{m}$), consistent with thermal softening of the cladding material.

The simulation with *thermal creep* shows a progressive approach between tube and grid during the first 7,000 hours due to positive radial creep strain. This continues until 27,780 hours when mechanical contact is achieved at the dimple (see Fig. 11(j-l)). Beyond this, the contact constrains deformation, and a slight separation forms on the opposite side due to bending effects.

In the case of *irradiation creep*, the CLR shows a quasi-linear increase once equilibrium is reached at approximately 1.2 dpa. This linear trend suggests that irradiation creep strain develops gradually and consistently with the applied load.

When *all phenomena are considered simultaneously*, the evolution is dominated by irradiation-induced effects, which produce significantly greater strain than thermal mechanisms. After the initial accommodation (1.2 dpa), a nearly linear separation trend is observed, reflecting the cumulative contribution of both irradiation growth and creep.

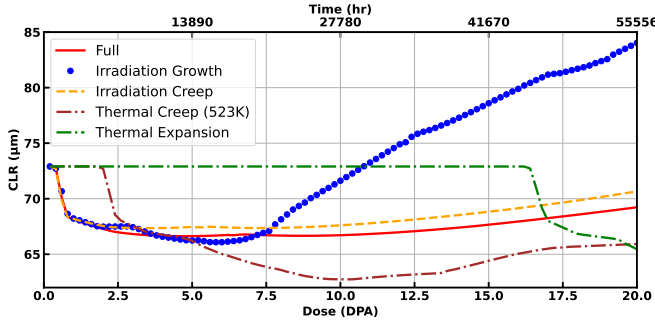


Fig. 5: Evolution of CLR distance under different physical mechanisms. The CLR is evaluated by isolating each phenomenon individually: irradiation growth (blue symbols), irradiation creep (orange dashed line), thermal expansion (green dash-dotted line), thermal creep (brown dash-dotted line), and the combined case with all active phenomena — full (red solid line).

Figures 6 and 7 further compare the evolution of the CLR at both sides of the spacer grid, considering cases with and without thermal effects. Figure 6 covers up to 20 dpa (55,556 hours), while Figure 7 extends the simulation to 40 dpa (111,120 hours).

The curves corresponding to simulations with and without thermal phenomena remain nearly parallel, indicating that thermal expansion and thermal creep introduce only minor deviations of grid and cladding interaction under the

conditions studied. These results confirm that irradiation-induced mechanisms, particularly irradiation creep and growth, are the dominant contributors to deformation and separation in the system.

Thermal effects, although limited for the current component geometry and operating conditions, were included to ensure a comprehensive assessment of the system behavior.

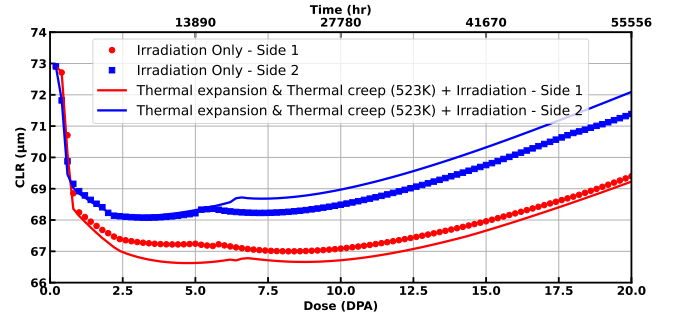


Fig. 6: Maximum CLR as a function of dose (DPA), comparing irradiation-only cases (symbols) and combined irradiation + thermal loading (lines), up to 20 dpa (55,556 hours).

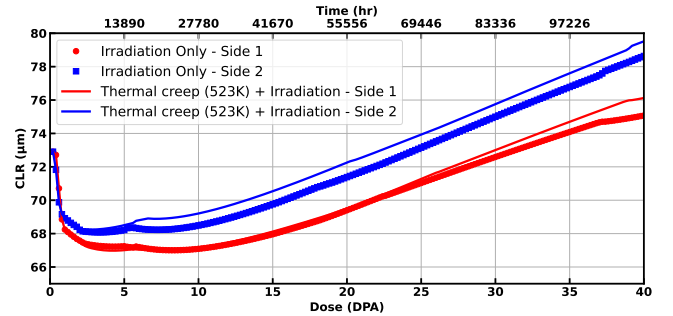


Fig. 7: Maximum CLR as a function of dose (DPA), comparing irradiation-only and coupled thermal+irradiation loading, up to 40 dpa (111,120 hours).

Introducing thermal effects into the model increases the computational cost significantly. While the cases considering only irradiation effects required approximately 4 to 6 hours to complete, the fully coupled simulations—accounting for both thermal and irradiation phenomena—took between 14 and 15 hours. All simulations were executed using MPI with 4 parallel processes on an AMD EPYC 7513 CPU running at 2.6 GHz. This increase in computational demand highlights the trade-off between physical fidelity and numerical cost when modeling coupled multiphysics scenarios.

4.3. Influence of the thermal effects on CLR

Two sensitivity analyses are carried out to assess the impact of the heating rate over the assembly mechanics. Figure 8 presents the evolution of the cladding-to-grid CLR over time considering only thermal expansion for different heating rates. The results indicate that higher ramp rates lead to an earlier onset of instability and contact between the cladding tube and the spacer grid, reaching a minimum CLR

of approximately $64 \mu\text{m}$. This is followed by a separation phase where the gap increases. As the heating rate increases, both the timing and steepness of the contact and separation phases become more pronounced.

Figure 9 shows the corresponding CLR evolution when only thermal creep is considered under the same heating rate scenarios. In this case, faster heating results in a smaller approach between tube and grid. This behavior is attributed to the higher creep strain rates generated by steeper thermal gradients and the compressive radial stress applied to the tube. Due to the crystallographic texture—particularly the alignment of prismatic planes perpendicular to the radial stress—a faster heating rate favors deformation along directions with lower resolved shear stress, thereby limiting radial displacement and reducing contact with the spacer grid.

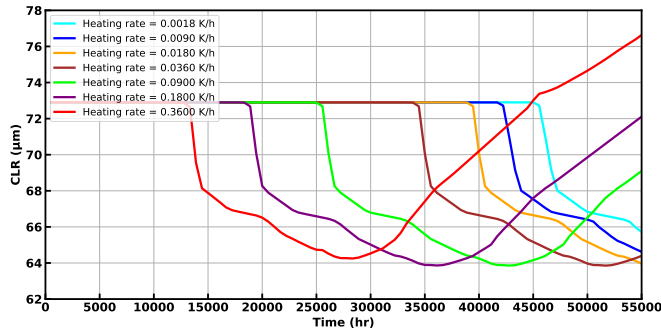


Fig. 8: Evolution of CLR under different heating rates considering only thermal expansion. Higher heating rates result in earlier and stronger separation phases.

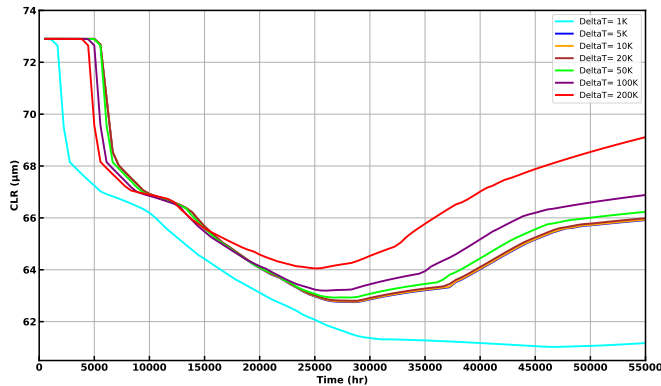


Fig. 9: CLR evolution under different heating rates considering only thermal creep. Increased heating rates reduce the overall approach due to enhanced strain rates and the specific crystallographic orientation of the cladding.

4.3.1. Thermal pre-load effect on irradiated components

This study compares two simulation scenarios: (1) without thermal pre-loading prior to irradiation, and (2) with thermal pre-loading ($\Delta T = 523\text{K}$) applied before irradiation, to evaluate its impact on the CLR evolution between the cladding tube and spacer grid.

This thermal pre-loading scenario is representative of conditions such as hot shutdowns or hot standbys in PWR, where the core remains at high temperature and pressure despite being subcritical. Under these circumstances, fuel components may undergo significant thermal expansion prior to irradiation, potentially influencing early-stage mechanical interaction.

Hence, thermal pre-loading induces initial thermal expansion, maintaining a near-constant CLR during early irradiation stages (up to $\approx 2\text{dpa}$), demonstrating predominantly elastic behavior. Beyond this threshold, nonlinearity emerges due to thermal creep softening, resulting in a gradual tube-grid approach (maximum clearance: $\approx 64 \mu\text{m}$). The dimple-tube geometry generates localized stress concentrations (see Fig. 5(j-l)), leading to asymmetric deformation with peak CLR ($\approx 76 \mu\text{m}$) at the dimple's opposite edge, as evidenced in Fig. 10 (post $\approx 8\text{dpa}$).

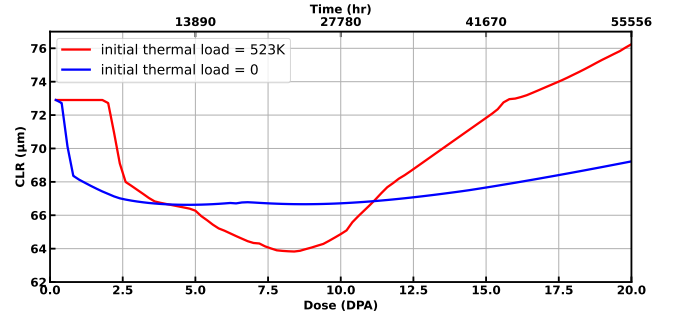


Fig. 10: Simulated CLR comparison for Side 1: red = with thermal pre-load ($\Delta T = 523\text{K}$), blue = without pre-load. Key features: (i) Pre-loaded case shows initial elastic regime ($< 2\text{dpa}$) followed by creep-driven approach $\approx 64 \mu\text{m}$; (ii) Non-preloaded case exhibits early separation ($0.5\text{--}1.2\text{dpa}$) then stabilization. Error bands: ($\pm 5 \mu\text{m}$).

In contrast, simulations without pre-loading exhibit early pivot-induced separation (initiated at $\approx 0.5\text{dpa}$, stabilized by $\approx 1.2\text{dpa}$), followed by CLR stabilization. While experimental validation remains pending, these results provide some key insights for dynamic fuel assembly interaction analysis, grid-to-cladding clearance optimization in design phases, irradiation-enhanced deformation mechanisms.

4.4. Detailed description of the spatial stress-strain distribution.

A more detailed description of the structural behavior is presented in Figure 11(a–f), which shows the distribution of von Mises (VM) strains (top row) and VM stresses (bottom row) under combined thermal and irradiation conditions. The analysis is divided into three cases: the first column corresponds to the scenario with irradiation effects only (irradiation creep and growth), the second column includes only thermal effects (thermal creep and thermal expansion with heating rate = 0.0018 K/h), and the third column represents the superposition of all phenomena.

When only irradiation mechanisms are considered, a localized plastic deformation of approximately 1.6×10^{-2} develops specifically in the region where the spring load is applied on the cadding tube, accompanied by VM stress concentrations reaching nearly 230 MPa. In contrast, when only thermal effects (thermal expansion and creep) are included, the deformation is significantly lower, reaching about 7.2×10^{-3} , with a corresponding VM stress of approximately 180 MPa. These results confirm the relatively minor contribution of thermal effects under the given loading conditions.

When all mechanisms act simultaneously—irradiation growth and creep, thermal expansion, and thermal creep—the resulting deformation in the loaded region increases to approximately 2.1×10^{-2} , representing a 31% increase in strain compared to the irradiation-only case. Meanwhile, the VM stress slightly decreases to 210 MPa in the spring load region. This suggests a localized stress relaxation effect, likely driven by the interplay between irradiation-induced strain and thermally activated material softening, which facilitates stress redistribution despite continued strain accumulation.

Figure 11(g–l) presents the local VM strain (top row) and stress (bottom row) distributions at the dimple contact region on Side 1, under different loading conditions. These local results complement the global response shown in (a–f). The first column shows the outcome with only irradiation effects (irradiation creep and growth), the second with only thermal effects (thermal creep and thermal expansion), and the third with both irradiation and thermal mechanisms combined.

When only irradiation effects are considered (first column), a localized strain of approximately 1.1×10^{-2} is observed at the contact points between the cladding tube and the grid dimples. In the same regions, VM stresses reach around 210 MPa. This behavior reflects the accumulation of irradiation-induced strain in the high-contact stress zones.

In contrast, when only thermal effects are considered (second column), the maximum localized strain is greater, reaching approximately 1.9×10^{-2} , while the VM stress slightly decreases to around 200 MPa.

When both thermal and irradiation effects are taken into account simultaneously (third column), the deformation field is dominated by the irradiation-induced strain, while thermal effects contribute mainly to the relaxation of stresses in the contact region.

4.4.1. Influence of elastic coefficients on stress and strain fields

The anisotropic elastic constants of zirconium as a function of temperature were determined by Fisher and Renken (1961, 1964) in a range spanning from 4 K to approximately 1100 K. Additionally, Tremblay and Roy (1973) studied the elastic constants of zirconium in an alloy with high oxygen content. It is well known that the presence of alloying elements modifies the lattice parameters and, consequently, affects the elastic constants.

In this work, the values reported by Douglass (1971) were used for the simulation of thermal expansion. At a

temperature of 576 K, the elastic constants employed were:

$$\begin{aligned} C_{11} &= 130.1 \text{ GPa}, & C_{33} &= 155.9 \text{ GPa}, \\ C_{44} &= 28.2 \text{ GPa}, & C_{12} &= 78.6 \text{ GPa}, & C_{13} &= 65.7 \text{ GPa}. \end{aligned}$$

Figures 12 present the distributions of VM elastic strains and stresses for two cases: (1) using room temperature elastic constants (see Section 2.1.4), and (2) using elastic constants at 576 K (see Section 4.4.1). A component-level comparison shows that the equivalent elastic strain reaches approximately 2.5×10^{-4} in the first case and 2.4×10^{-4} in the second. The equivalent VM stress remains nearly identical in both simulations, with a maximum of approximately 210 MPa.

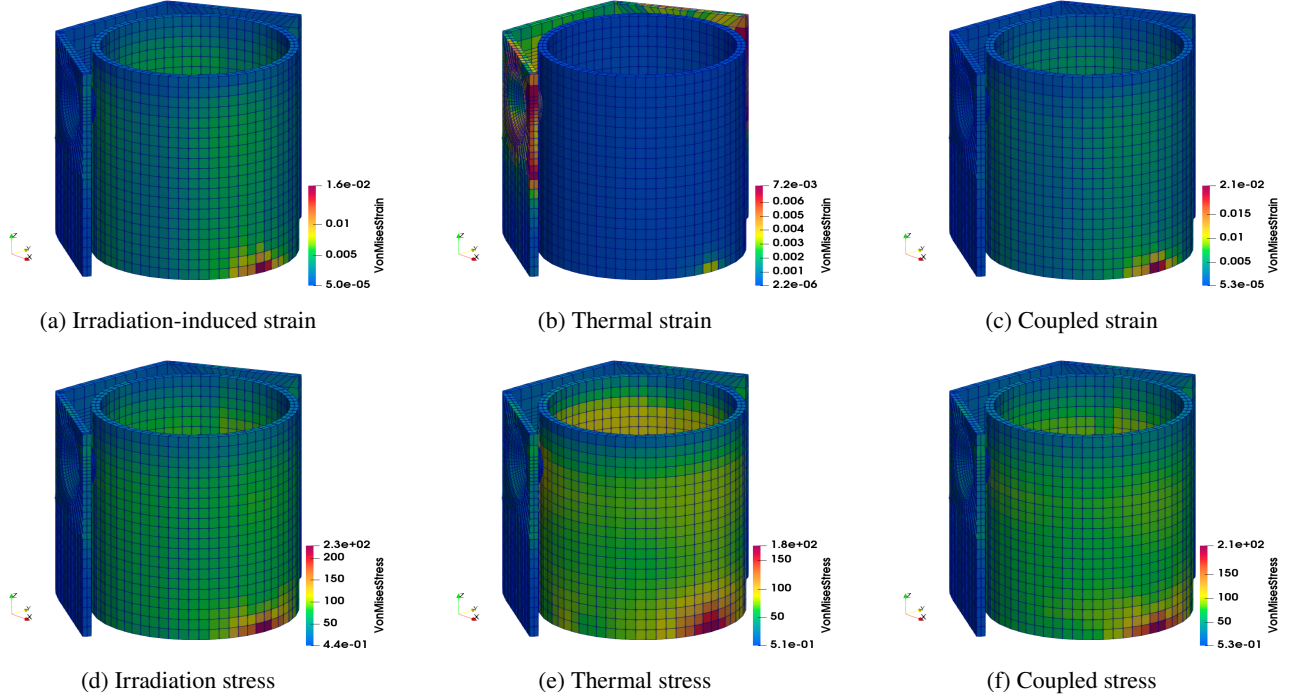
In particular, the comparison suggests that the thermal effects on the the elastic constants contribute to stress relaxation and increase deformation on the early stages (see Fig. 11d–f). This can be explained by means of the reduction of the elastic coefficients corresponding to 576 K, that promote greater localized deformation compared to those of the cold-worked state. This indicates that temperature impacts the material response mainly through micromechanical phenomena, rather than through the temperature dependence of the elastic constants alone. This effect is further illustrated in Figure 13, which compares the CLR between the cladding tube and spacer grid for both sets of elastic coefficients. While the stress and strain fields show negligible differences, the use of coefficients at 576 K produces a relative approach of approximately 2 μm , suggesting a non-negligible influence of elastic stiffness on contact evolution.

5. Conclusion

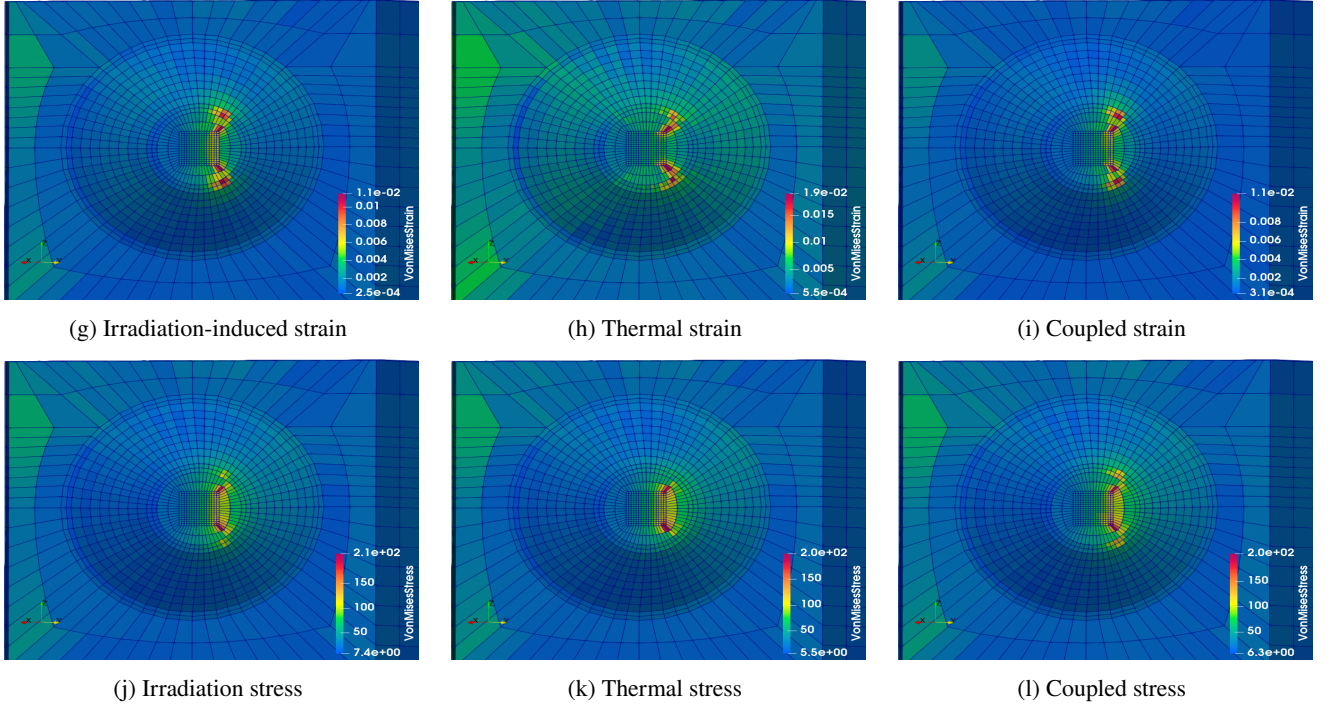
This work incorporates thermally activated mechanisms such as creep and expansion within the CAFEM-VPSC interface developed in (Aguzzi et al., 2025) to simulate irradiated component assemblies under typical PWR conditions. The numerical results support the following conclusions:

1. **Thermal creep is stress-sensitive and leads to higher strain under steady-state conditions:** The analysis confirms that, for a given stress level, total strain increases consistently when thermal effects are included. At 523 K under an axial load of 200 MPa, the axial strain rises from 0.018 (only irradiation effects at 20 dpa) to 0.027 when thermal creep and expansion are also considered—representing a 50% increase. This highlights the stress-dependent nature of thermal creep and its relevance for modeling cladding deformation under standard reactor operating conditions.
2. **Thermal effect impact to CLR evolution:** For this specific spacer grid–cladding configuration and operation conditions, thermally induced deformations (creep and expansion) exhibit a very small influence on contact dynamics, with CLR variations remaining below 1% compared to irradiation-dominated scenarios. However, thermal preloading (e.g., $\Delta T = 523 \text{ K}$) alters the initial gap stability, accelerating tube-to-grid

(a)–(f) Global response (cladding + spacer grid)



(g)–(l) Local response at dimple contact (Side 1)


Fig. 11: VM elastic strain and stress distributions under different loading conditions. (a–f): Global response. (g–l): Local response.

contact recovery. This early contact onset could enhance mechanical stability by mitigating flow-induced vibration risks during initial reactor operation. This phenomenon would be relevant within a modal analysis on these components.

3. **Stress relaxation under full coupling:** The structural analysis (Section 4.4) showed that the inclusion of thermal effects results in higher von Mises strains but lower stress levels compared to the irradiation-only case. This behavior is attributed to material softening and stress relaxation driven by thermal activation,

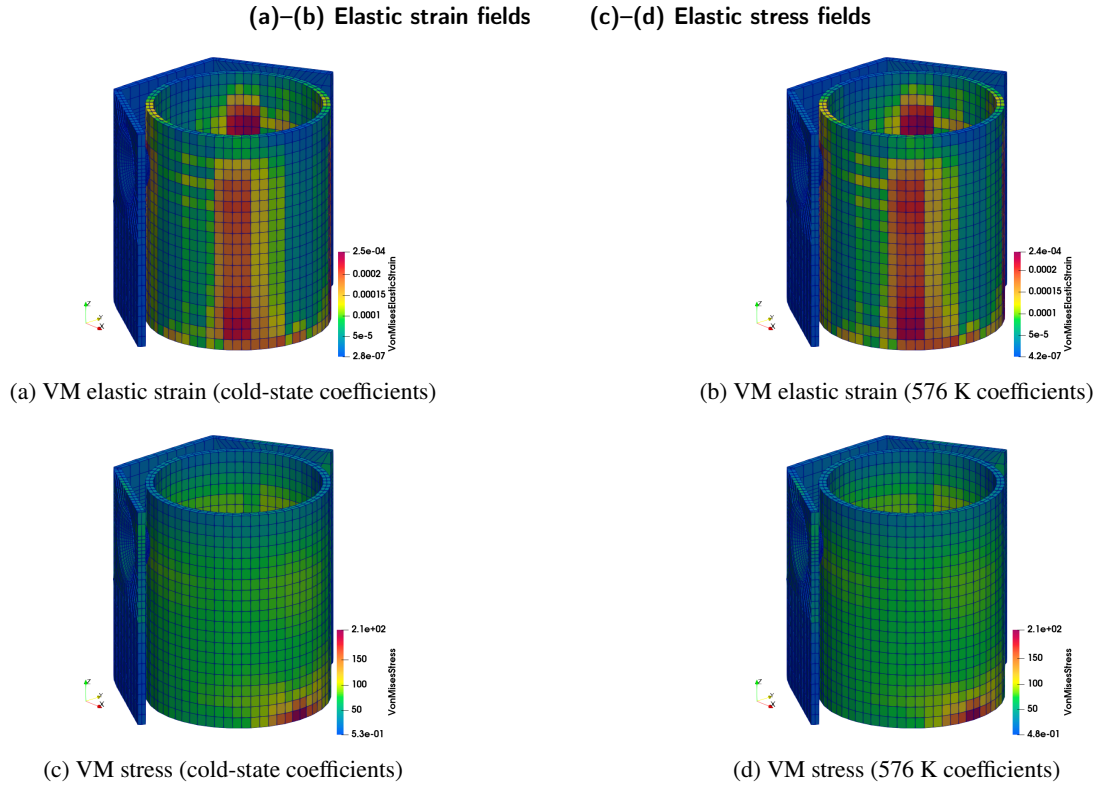


Fig. 12: Global distributions of VM elastic strain and stress in the full assembly (cladding tube + spacer grid) under coupled irradiation and thermal loading. (a–b): Strain fields using elastic coefficients at room temperature and 576 K, respectively. (c–d): Corresponding stress fields. Results highlight the influence of elastic moduli selection on local deformation and stress distribution.

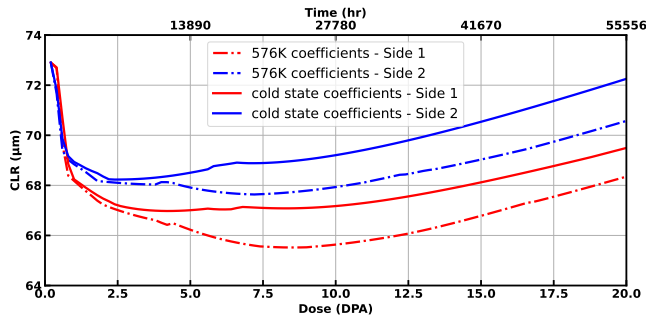


Fig. 13: Influence of elastic coefficients on CLR between the cladding tube and spacer grid.

particularly due to the predominant orientation of prismatic slip systems aligned with the radial load.

4. **Strain–stress fields driven by micromechanics over elasticity:** The simulated strain and stress fields were more sensitive to micromechanical behavior (slip activity and defect accumulation) than to the choice of elastic constants (Section 4.4.1). This is partly influenced by the boundary condition strategy used: the internal nodes on the free end of the cladding were tied to a fictitious remote node, which facilitates displacement toward the grid under spring loading. Future

work should focus on calibrating the stiffness of this constraint to improve physical representativeness.

This crystal plasticity-based methodology provides significant insight into the stress–strain response and mechanical interaction of fuel components. Even though in the current application the clearance could be properly estimated by irradiation models, the thermal effects impact significantly in the local integrity of the components. Hence, the full model serves as a *computational tool* capable of extrapolating microscale results to phenomenological models with lower computational demand. This practice opens possibilities for simulating more complex reactor internal geometries in industrial applications, achieving a realistic approximation of material behavior with significantly reduced time and cost.

CRediT authorship contribution statement

F. E. Aguzzi: Methodology, Software, Formal analysis, Writing. S. M. Rabazzi: Software, Formal analysis. M. S. Armoa: Methodology, Writing. C. I. Pairetti: Supervision, Formal analysis, Writing - review & editing. A. E. Albanesi: Supervision, Formal analysis, Writing - review & editing.

Table 1

Model parameters for Zircaloy-2, from Patra et al. (2017b) and Patra et al. (2017a).

Parameter	Value	Meaning
C_{11}, C_{22}, C_{33}	143.5, 143.5, 164.9	Elastic constants in GPa (assumed to be the same as that for pure Zr). Values taken from Simmons (1965) and Kocks <i>et al.</i> (2000).
C_{12}, C_{13}, C_{23}	72.5, 65.4, 65.4	
C_{44}, C_{55}, C_{66}	32.1, 32.1, 35.5	
f_r	0.97	Fraction of point defects that recombine during the cascade
f_{ic}	0.13	Fraction of interstitials that form clusters
B	$5.0 \times 10^{-5} \text{ MPa-dpa}^{-1}$	Crystallographic irradiation creep compliance
p_{ref}	$2.26 \times 10^{14} \text{ m}^{-2}$	Weighting factor for line dislocation density in irradiation creep model
$b^j, j = \alpha_1, \alpha_2, \alpha_3$	$3.0 \times 10^{-10} \text{ m}$	Magnitude of Burgers vector along the prismatic directions
$b^j, j = c$	$5.0 \times 10^{-10} \text{ m}$	Magnitude of Burgers vector along the basal direction

Declaration of competing interest

The authors declare that they have no known competing financial interests or personal relationships that could have appeared to influence the work reported in this paper.

Acknowledgments

The authors gratefully acknowledge the financial support from CONICET (Argentine Council for Scientific and Technical Research) and the National Agency of Scientific and Technological Promotion of Argentina (ANPCYT) for the Grant PICT-2020-SERIEA-03475. The authors also acknowledge computer time provided by CCT-Rosario Computational Center, member of the High Performance Computing National System (SNCAD, ME-Argentina).

Appendix A: Material parameters

The material parameters presented in Table 1 were taken from Patra et al. (2017b) and Patra et al. (2017a).

Appendix B: Validation benchmark

A benchmark case was used to verify the implementation of the thermal creep phenomenon in the Code_Aster–VPSC coupling. This involved a code-to-code comparison against results obtained with the stand-alone VPSC code. The conditions of the reference case are summarized in Table 2. The simulation was performed using a single three-dimensional eight-node finite element under constant stress. The results of the comparison between Code_Aster–VPSC and stand-alone VPSC are shown in Figure 14.

Table 2

Simulation conditions for thermal creep tests.

Description	Temp. (K)	Stress (MPa)	Texture
Thermal Creep	523	10 (22)	(0,0,0)*

*Euler angles: rotation around Z, then X, then Z axis.

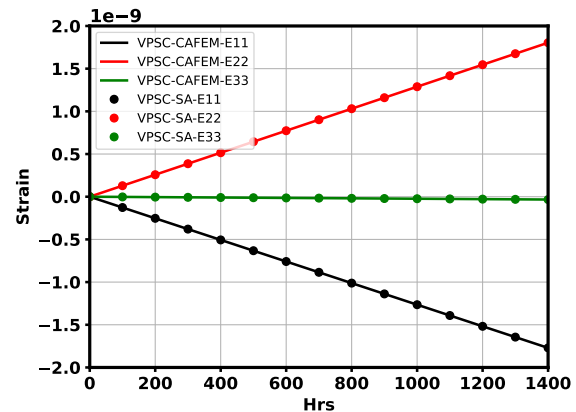


Fig. 14: Thermal strain at 523 K for single crystal with 10 MPa applied along direction 22. Symbols represent standalone VPSC results; solid lines correspond to Code Aster–VPSC predictions.

References

- Adamson, R., Garzarolli, F., Patterson, C., 2009. In-reactor creep of zirconium alloys. Advanced Nuclear Technology International.
- Adamson, R.B., Coleman, C.E., Griffiths, M., 2019. Irradiation creep and growth of zirconium alloys: A critical review. Journal of Nuclear Materials 521, 167–244.
- Aguzzi, F., Rabazzi, S.M., Armoa, M., Pairetti, C., Albanesi, A.E., 2025. An open-source finite element toolbox for anisotropic creep and irradiation growth: Application to cladding tube and spacer grid. Nuclear Engineering and Design (<https://doi.org/10.1016/j.nucengdes.2025.114345>).
- Aguzzi, F.E., Signorelli, J.W., 2024. Integración del modelo visco-plástico autoconsistente con leyes bajo irradiación de creep y crecimiento en el código de elementos finitos Code_Aster, in: XL Congreso Argentino de

- Mecánica Computacional.
- Billerey, A., 2005. Evolution of fuel rod support under irradiation–Impact on the mechanical behaviour of fuel assemblies. Structural behaviour of fuel assemblies for water cooled reactors, 101–111.
- Brenner, R., Masson, R., Castelnau, O., Zaoui, A., 2002. A “quasi-elastic” affine formulation for the homogenised behaviour of nonlinear viscoelastic polycrystals and composites. European Journal of Mechanics A/Solids 21 (6), 943–960.
- Butcher, F.J., Donohue, S.A., 1986. In-reactor deformation of cold-drawn tubes of Zr-2.5 wt% Nb. CNRL, CNRL-4022.
- Carpenter, G.J.C., Zee, R.H., Rogerson, A., 1988. Irradiation growth of zirconium single crystals: A review. Journal of Nuclear Materials 159, 86–100.
- CONUAR, 2025. CONUAR - Combustibles Nucleares Argentinos. <https://www.conuar.ar/>.
- Christodoulou, N., Chow, C.K., Turner, P.A., Tomé, C.N., Klassen, R.J., 2002. Analysis of steady-state thermal creep of Zr-2.5 Nb pressure tube material. Metallurgical and Materials Transactions A 33, 1103–1115.
- Christodoulou, N., Causey, A.R., Holt, R.A., Tomé, C.N., Badie, N., Klassen, R.J., Sauvé, R., Woo, C.H., 1996. Modeling in-reactor deformation of Zr-2.5 Nb pressure tubes in CANDU power reactors. Zirconium in the Nuclear Industry: Eleventh International Symposium, ASTM International.
- Douglass, D.L., 1971. The metallurgy of zirconium. Atomic energy review. EDF, 1989–2025. Electricité de France. Finite element *code_aster*, Analysis of Structures and Thermomechanics for Studies and Research. Open source on www.code-aster.org.
- Ehrlich, K., 1981. Irradiation creep and interrelation with swelling in austenitic stainless steels. Journal of nuclear materials 100, 1-3, 149–166.
- Fidleris, V., 1988. The irradiation creep and growth phenomena. Journal of Nuclear Materials 159, 22–42.
- Fisher, E.S., Renken, C.J., 1961. Adiabatic elastic moduli of single crystal alpha zirconium. Journal of Nuclear Materials 4, 3, 311–315.
- Fisher, E.S., Renken, C.J., 1964. Single-crystal elastic moduli and the hcp→bcc transformation in Ti, Zr, and Hf. Physical review 135, 2A, A482.
- Foster, J.P., Wolfer, W.G., Biancheria, A., Boltax, A., 1972. Analysis of irradiation-induced creep of stainless steel in fast spectrum reactors. Westinghouse Electric Corp.
- Franklin, D.G., Lucas, G.E., Bement, A.L., 1983. Creep of zirconium alloys in nuclear reactors. ASTM International, STP 815.
- Gicquel, C., Onimus, F., Brenner, R., Helfer, T., Masson, R., 2023. Polycrystalline simulations of in-reactor deformation of zircaloy-4 cladding tubes during nominal operating conditions. Zirconium in the Nuclear Industry: 20th International Symposium, 118–148.
- Goldak, J., Lloyd, L.T., Barrett, C.S., 1966. Lattice parameters, thermal expansions, and Grüneisen coefficients of Zirconium, 4.2 to 1130 K. Physical Review 144, 2, 478.
- Hayes, T.A., Kassner, M.E., 2006. Creep of zirconium and zirconium alloys. Metallurgical and Materials Transactions A 37, 2389–2396.
- Holt, R.A., Causey, A.R., Christodoulou, N., Griffiths, M., Ho, E.T.C., Woo, C.H., 1996. Non-linear irradiation growth of cold-worked Zircaloy-2. ASTM Special Technical Publication 1295, 623–637.
- Holt, R.A., 2008. In-reactor deformation of cold-worked Zr–2.5 Nb pressure tubes. Journal of Nuclear Materials 372, 2-3, 182–214.
- Jiang, H., Qu, J., Lu, R.Y., Wang, J.J., 2016. Grid-to-rod flow-induced impact study for PWR fuel in reactor. Progress in Nuclear Energy 91, 355–361.
- Joulin, T.P., Gue'rou, F.M., Lina, A., Moinereau, D., 2002. Effects of loading conditions and types of motion on PWR fuel rod cladding wear. ASME International Mechanical Engineering Congress and Exposition, 36592, 1011–1018.
- Kocks, U.F., Tomé, C.N., & Wenk, H.-R., 2000. Texture and anisotropy: preferred orientations in polycrystals and their effect on materials properties. Cambridge University Press. ISBN 978-0-521-79420-6.
- Lebensohn, R.A., Tomé, C.N., 1993. A self-consistent anisotropic approach for the simulation of plastic deformation and texture development of polycrystals: application to zirconium alloys. Acta metallurgica et materialia 41, 9, 2611–2624.
- Limbäck, M., Andersson, T., 1996. A model for analysis of the effect of final annealing on the in-and out-of-reactor creep behavior of zircaloy cladding. Zirconium in the Nuclear Industry: Eleventh International Symposium.
- Matsuo, Y., 1987. Thermal creep of zircaloy-4 cladding under internal pressure. Journal of Nuclear Science and Technology 24, 2, 111–119.
- McGinty, R.D., 2001. Multiscale representation of polycrystalline inelasticity. Georgia institute of technology.
- Molinari, A., Canova, G.R., Ahzi, S., 1987. A self consistent approach of the large deformation polycrystal viscoplasticity. Acta Metallurgica 35, 12, 2983–2994.
- Montgomery, R., Tomé, C., Liu, W., Alankar, A., Subramanian, G., Stanek, C., 2017. Use of multiscale zirconium alloy deformation models in nuclear fuel behavior analysis. Journal of Computational Physics 328, 278–300.
- Moore, B., Topping, M., Long, F., Daymond, M.R., 2025. Stress and temperature dependence of irradiation creep in zircaloy-4 studied using proton irradiation. Journal of Nuclear Materials 603, 155383.
- Murty, K.L., 1999. Creep studies for zircaloy life prediction in water reactors. JOM 51, 32–39.
- Norgett, M.J., Robinson, M.T., Torrens, I.M., 1975. A proposed method of calculating displacement dose rates. Nuclear engineering and design 33, 1, 50–54.
- Onimus, F., Doriot, S., Béchade, J.L., 2020. Radiation effects in zirconium alloys. Comprehensive nuclear materials 3, 1–56.
- Onimus, F., Gelebart, L., Brenner, R., 2022. Polycrystalline simulations using Fast Fourier Transform method of in-reactor deformation of recrystallized Zircaloy-4 tubes. Numat2022-The Nuclear Materials Conference.
- Onimus, F., Doriot, S., Béchade, J.L., 2020. Radiation effects in zirconium alloys. Comprehensive nuclear materials 3, 1–56.
- Patra, A., Tomé, C.N., 2017. Finite element simulation of gap opening between cladding tube and spacer grid in a fuel rod assembly using crystallographic models of irradiation growth and creep. Nuclear Engineering and Design 315, 155–169.
- Patra, A., Tomé, C.N., Golubov, S.I., 2017. Crystal plasticity modeling of irradiation growth in Zircaloy-2. Philosophical Magazine 97, 23, 2018–2051.
- Rogerson, A., 1988. Irradiation growth in zirconium and its alloys. Journal of Nuclear Materials 159, 43–61.
- Segurado, J., Lebensohn, R.A., LLorca, J., Tomé, C.N., 2012. Multi-scale modeling of plasticity based on embedding the viscoplastic self-consistent formulation in implicit finite elements. International Journal of Plasticity 28, 1, 124–140.
- Simmons, G., 1965. Single crystal elastic constants and calculated aggregate properties. Journal of the Graduate Research Center 34, 1, 1.
- Sleight, A.W., 1998. Isotropic negative thermal expansion. Annual review of materials science 28, 1, 29–43.
- Tomé, C.N., So, C.B., Woo, C.H., 1993. Self-consistent calculation of steady-state creep and growth in textured zirconium. Philosophical magazine A 67, 4, 917–930.
- Tomé, C.N., Christodoulou, N., Turner, P.A., Miller, M.A., Woo, C.H., Root, J., Holden, T.M., 1996. Role of internal stresses in the transient of irradiation growth of Zircaloy-2. Journal of nuclear materials 227, 3, 237–250.
- Tomé, C.N., Lebensohn, R.A., 2023. Material modeling with the viscoplastic self-consistent (VPSC) approach: theory and practical applications. Elsevier.
- Tremblay, M., Roy, C., 1973. Elastic parameters of single crystal Zr-O alloys. Materials Science and Engineering 12, 5-6, 235–243.
- Turner, P.A., Tomé, C.N., 1993. Self-consistent modeling of visco-elastic polycrystals: application to irradiation creep and growth. Journal of the Mechanics and Physics of Solids 41, 7, 1191–1211.
- Turner, P.A., Tomé, C.N., Woo, C.H., 1994. Self-consistent modelling of nonlinear visco-elastic polycrystals: an approximate scheme. Philosophical Magazine A 70, 4, 689–711.

- Turner, P.A., Tomé, C.N., Christodoulou, N., Woo, C.H., 1999. A self-consistent model for polycrystals undergoing simultaneous irradiation and thermal creep. *Philosophical Magazine A* 79, 10, 2505–2524.
- Wang, H., Hu, Z., Lu, W., Thouless, M.D., 2013. A mechanism-based framework for the numerical analysis of creep in zircaloy-4. *Journal of Nuclear Materials* 433, 1-3, 188–198.
- Woo, C.H., 1985. Polycrystalline effects on irradiation creep and growth in textured zirconium. *Journal of Nuclear Materials* 131, 2-3, 105–117.
- Xiao, X., Xie, H., Li, S., Yu, L., 2023. Modelling thermal and irradiation creep with crystal plasticity theory and self-consistent method. *Journal of Nuclear Materials* 587, 154702.
- U2.04.04, 2024. The Code_Aster mesh file. <https://biba1632.gitlab.io/code-aster-manuals/docs/user/u2.04.04.html>.